Descriptor-Type Kalman Filter and TLS EXIN Speed Estimate for Sensorless Control of a Linear Induction Motor

Francesco Alonge, *Member, IEEE*, Maurizio Cirrincione, *Senior Member, IEEE*, Filippo D'Ippolito, *Member, IEEE*, Marcello Pucci, *Senior Member, IEEE*, Antonino Sferlazza, *Student Member, IEEE*, and Gianpaolo Vitale, *Senior Member, IEEE*

***Abstract*—This paper proposes a speed observer for linear induction motors (LIMs), which is composed of two parts: 1) a linear Kalman filter (KF) for the online estimation of the inductor currents and induced part flux linkage components; and 2) a speed estimator based on the total least squares (TLS) EXIN neuron. The TLS estimator receives as inputs the state variables, estimated by the KF, and provides as output the LIM linear speed, which is fed back to the KF and the control system. The KF is based on the classic space-vector model of the rotating induction machine. The end effects of the LIMs have been considered an uncertainty treated by the KF. The TLS EXIN neuron has been used to compute, in recursive form, the machine linear speed online since it is the only neural network able to solve online, in a recursive form, a TLS problem. The proposed KF TLS speed estimator has been tested experimentally on a suitably developed test setup, and it has been compared with the classic extended KF.**

***Index Terms*—Kalman filter (KF), linear induction motor (LIM), neural networks (NNs), total least squares (TLS).**

NOMENCLATURE

u_{sD}, u_{sQ}	Inductor voltages in the inductor reference frame.
i_{sD}, i_{sQ}	Inductor currents in the inductor reference frame.
i_{sx}, i_{sy}	Inductor current in the induced part flux oriented reference frame.
ψ_{rd}, ψ_{rq}	Induced part fluxes in the inductor reference frame.
$L_s(L_r)$	Inductor (induced part) inductance.
L_m	Three-phase magnetizing inductance.
$R_s(R_r)$	Inductor (induced part) resistance.
$T_r = \frac{L_r}{R_r}$	Induced part time constant.
σ	Total leakage factor.
ω_r	Electrical angular speed.
v	Mechanic linear speed.
p	Pole-pairs.
τ_p	Pole-pitch.
T_s	Sampling time.
F_e	Electromagnetic thrust.

I. INTRODUCTION

SCIENTIFIC literature about linear induction motors (LIMs) is huge [1], [2]. The feature of LIMs to develop a direct linear motion without any gearbox for the motion transformation (from rotating to linear) has been the key issue for their study. The counterpart of this potential advantage is the increase in the complexity of the machine model, which presents the so-called end effects and border effects, which are due to the absence of a cylindrical symmetry in the inductor structure with respect to the rotating machine, both in the longitudinal and transversal directions. This results in difficulties in obtaining good dynamic performance. Speed control of LIMs, moreover, requires the adoption of a linear encoder, which is typically more expensive and less reliable than the corresponding counterpart in the rotating machine. As a matter of fact, in the LIM case, the cost of the encoder increases with the length of the induced part track, which could be prohibitive in applications such as railway traction systems and, in general, movement systems with long tracks. The possibility of adopting suitable sensorless techniques [3], [4] is therefore very interesting for these applications, where the linear encoder might be also generally exposed to potentially damaging environmental factors (sun, humidity, mechanical stress, etc.). So far, very few applications of sensorless techniques suitable for

Manuscript received May 21, 2013; revised September 9, 2013; accepted April 1, 2014. Date of publication April 10, 2014; date of current version November 18, 2014. Paper 2013-IDC-195.R1, presented at the 2012 IEEE Symposium on Sensorless Control for Electrical Drives, Milwaukee, WI, USA, September 21–22, and approved for publication in the IEEE TRANSACTIONS ON INDUSTRY APPLICATIONS by the Industrial Drives Committee of the IEEE Industry Applications Society. This work was supported by the following research projects: 1) RITmare, Ricerca ITaliana per il mare (Italian Research for the sea) CUP: B91J11000740001; 2) TESEO, Tecnologie ad alta Efficienza per la Sostenibilità Energetica ed ambientale On-board (High efficiency technologies for on-board energy and environmental sustainability) CUP: B61C12000850005; and 3) CNR per il Mezzogiorno (Advanced Technologies for Energy Efficiency and Sustainable Mobility) CUP: B51J10001290001.

F. Alonge and F. D'Ippolito are with the Department of Energy Information Engineering and Mathematical Models, University of Palermo, 90128 Palermo, Italy (e-mail: francesco.alonge@unipa.it; filippo.dippolito@unipa.it).

M. Cirrincione is with the School of Engineering and Physics (SEP), University of the South Pacific, Laucala Campus, Suva, Fiji Islands, and with the University of Technology of Belfort Montbeliard, 90400 Belfort, France, and also with the Laboratoires OPERA/FCLAB FRCNRS3539, 90010 Belfort, France (e-mail: maurizio.cirrincione@utbm.fr).

M. Pucci and G. Vitale are with the Institute on Intelligent Systems for Automation, Section of Palermo, National Research Council of Italy, 90128 Palermo, Italy (e-mail: pucci@pa.issia.cnr.it; vitale@pa.issia.cnr.it).

A. Sferlazza is with the Department of Energy Information Engineering and Mathematical Models, University of Palermo, 90128 Palermo, Italy, and also with the Institute of Intelligent Systems for Automation, National Research Council of Italy, 90128 Palermo, Italy (e-mail: antonino.sferlazza@unipa.it).

Color versions of one or more of the figures in this paper are available online at http://ieeexplore.ieee.org.

Digital Object Identifier 10.1109/TIA.2014.2316367

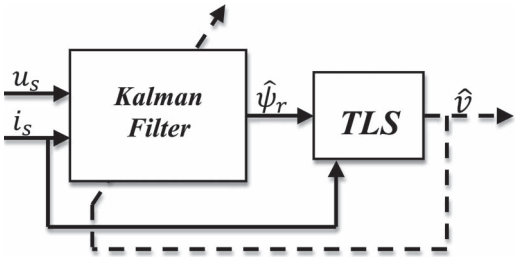

Fig. 1. Block diagram of the observer.

LIMs have been proposed in literature, among which are [5] and [6], probably because of the increased complexity of the speed observer, which should also consider the end effects of the machine. In particular, in [5], a complex adaptive speed sensorless controller for the LIM was proposed, whereas in [6], a sensorless technique for LIMs based on high-frequency signal injection was presented. In general, these last techniques are difficult to be applied to LIMs since there is no slotting effect in the induced part track and the saturation of the main flux is hard to be tracked. A completely different approach has been followed in [7] and [8] proposing, respectively, in numerical simulation and with experimental results, a neural network (NN) model reference adaptive system (MRAS) observer; this observer is characterized by the fact that the adaptive model is a linear NN trained online by the total least squares (TLS) EXIN neuron [9], [10]. This paper proposes a TLS-EXIN-based Kalman filter (KF) speed observer for LIMs. This observer is made up of two parts: 1) a KF; and 2) a speed estimator based on the TLS EXIN neuron [9]–[15].

The LIM, unlike the rotating induction motor (RIM), presents the so-called end effects. This suggests either the use of a suitable dynamic model considering the dynamic end effects [31], or the use of a RIM model where any mismatch with the behavior of a real LIM is considered noise; in other words, the end effects are included in additive noise terms. This can be done by using a KF. However, if all of the states of the model are estimated, the extended KF (EKF) should be used since the model is nonlinear. If, on the other hand, the linear speed of the LIM is considered a parameter, then a classical linear KF can be used, if accompanied by an online speed estimator.

In particular, the KF is used for online estimation of the machine state variables (inductor currents and induced part flux linkage components) and is based on the classic space-vector two equations of the RIM. The speed estimator is implemented by the TLS EXIN estimator, which receives as inputs the state variables estimated by the KF and provides as output the linear LIM speed, which is fed back to the KF and the control system, as shown in Fig. 1.

The TLS EXIN neuron has been used to compute online, in recursive form, the machine linear speed since it is the only NN able to solve online, in a recursive form, a TLS problem. The TLS EXIN neuron thus does not need any *a priori* training or learning phase, such as the classic multilayer perceptron trained by the backpropagation algorithm. The use of the TLS EXIN neuron permits the speed not to be estimated by the KF, leading up to a meaningful reduction of the computation effort in comparison with an estimation of all the variables, including speed, which is the case of the EKF. The proposed TLS KF speed observer has been tested experimentally on a suitably developed test setup. Results have been further compared experimentally with those achievable with the EKF.

II. Space-Vector Model of the LIM

The well-known dynamical model of the rotating induction motor is given by

$$\sigma L_s \frac{di_{sD}}{dt} + \frac{L_m}{L_r}\frac{d\psi_{rd}}{dt} = -R_s i_{sD} + u_{sD} \tag{1}$$

$$\sigma L_s \frac{di_{sQ}}{dt} + \frac{L_m}{L_r}\frac{d\psi_{rq}}{dt} = -R_s i_{sQ} + u_{sQ} \tag{2}$$

$$\frac{d\psi_{rd}}{dt} = \frac{L_m}{T_r} i_{sD} - \frac{1}{T_r}\psi_{rd} - \omega_r \psi_{rq} \tag{3}$$

$$\frac{d\psi_{rq}}{dt} = \frac{L_m}{T_r} i_{sQ} - \frac{1}{T_r}\psi_{rq} + \omega_r \psi_{rd} \tag{4}$$

$$F_e = \frac{3}{2}\frac{\pi p}{\tau_p}\frac{L_m}{L_r}(\psi_{rd} i_{sQ} - \psi_{rq} i_{sD}) \tag{5}$$

where F_e is the electromagnetic thrust of the LIM, which is computed neglecting the LIM end effects.

However, the model (1)–(5) also describes a LIM model if the end effects of this motor are not taken into consideration, putting $\omega_r = p(\pi/\tau_p)v$. For designing the KF, the descriptor form of the stochastic electromagnetic model has been developed, where the matrix that premultiplies vector $\dot{\boldsymbol{x}}(t)$ is a suitable matrix instead of an identity one as it occurs in a standard state-space form. (The reasons for using this descriptor form is explained in Remark 1.) Therefore, $\boldsymbol{x}(t)$, $\boldsymbol{u}(t)$, and $\boldsymbol{z}(t)$ as the state, input, and output vectors, respectively, are defined as

$$\boldsymbol{x} = [i_{sD} \quad i_{sQ} \quad \psi_{rd} \quad \psi_{rq}]^T \quad \boldsymbol{u} = [u_{sD} \quad u_{sQ}]^T$$
$$\boldsymbol{z} = [i_{sD}\ i_{sQ}]^T.$$

The descriptor form of (1)–(4) is given by

$$\boldsymbol{E}\dot{\boldsymbol{x}}(t) = \tilde{\boldsymbol{F}}(t)\boldsymbol{x}(t) + \tilde{\boldsymbol{B}}\boldsymbol{u}(t) + \tilde{\boldsymbol{Q}}\boldsymbol{w}(t) \tag{6}$$

$$\boldsymbol{z}(t) = \boldsymbol{H}\boldsymbol{x}(t) + \boldsymbol{R}\boldsymbol{s}(t) \tag{7}$$

where $\boldsymbol{w}(t)$ and $\boldsymbol{s}(t)$ are the system noise and measurement noise assumed zero-mean white noise uncorrelated between them and with the other variables and having covariance matrices equal to

$$\mathbb{E}\left\{\begin{bmatrix} s(t) \\ w(t) \end{bmatrix}\begin{bmatrix} s(t+\tau) \\ w(t+\tau) \end{bmatrix}^T\right\} = \begin{bmatrix} \delta_\tau & 0 \\ 0 & \delta_\tau \end{bmatrix} \tag{8}$$

where δ_τ is the unit sample sequence. $\tilde{\boldsymbol{Q}}$ and $\boldsymbol{R}$ are diagonal square matrices of suitable dimensions and represent the impact of the two uncorrelated noise vectors $\boldsymbol{w}(t)$ and $\boldsymbol{s}(t)$ on

$\boldsymbol{x}(t)$ and $\boldsymbol{z}(t)$, respectively. Matrices $\boldsymbol{E}$, $\tilde{\boldsymbol{B}}$, $\tilde{\boldsymbol{F}}(t)$, and $\boldsymbol{H}$ are given by

$$\boldsymbol{E} = \begin{bmatrix} \sigma L_s & 0 & \frac{Lm}{Lr} & 0 \\ 0 & \sigma L_s & 0 & \frac{Lm}{Lr} \\ 0 & 0 & 1 & 0 \\ 0 & 0 & 0 & 1 \end{bmatrix}$$

$$\tilde{\boldsymbol{B}} = \begin{bmatrix} 1 & 0 \\ 0 & 1 \\ 0 & 0 \\ 0 & 0 \end{bmatrix}$$

$$\tilde{\boldsymbol{F}}(t) = \begin{bmatrix} -R_s & 0 & 0 & 0 \\ 0 & -R_s & 0 & 0 \\ \frac{Lm}{Tr} & 0 & -\frac{1}{T_r} & -p\frac{\pi}{\tau_p}v(t) \\ 0 & \frac{Lm}{Tr} & p\frac{\pi}{\tau_p}v(t) & -\frac{1}{T_r} \end{bmatrix}$$

$$\boldsymbol{H} = \begin{bmatrix} 1 & 0 \\ 0 & 1 \\ 0 & 1 \\ 0 & 0 \end{bmatrix}^T.$$

Remark 1: The descriptor form has been chosen because the coefficients of the matrices appearing in the model (6) and (7) are simple expressions in terms of the physical parameters of the motor. This choice is justified from the consideration that the "descriptor"-type formulation is ideal for taking into consideration parameter variations inside the observer, such as for example a robust observer. The choice of the descriptor form permits the uncertainty of the model to be easily expressed in terms of the parameter variations. This is, however, out of the scope of this paper.

Remark 2: Matrix $\tilde{\boldsymbol{F}}(t)$ is time-varying because it depends on speed $v(t)$. Matrix $\boldsymbol{E}$ is nonsingular in all operating conditions, thus ensuring that the model (6) and (7) is equivalent to the model in a standard state-space form obtained premultiplying (6) for $\boldsymbol{E}^{-1}$.

Remark 3: The parameters of the electrical model have been obtained by the identification procedure described in [16], in which a simple and effective technique for parameter estimation of a linear induction machine is proposed.

Remark 4: Speed $v(t)$ is not considered a state, as in the EKF described in [16], but it is regarded as a parameter of the model. This results in a reduction of the order of the problem, with an increase in the efficiency of the algorithm.

Starting from the model (6) and (7), the following discrete-time fouth-order stochastic model is obtained by using the Euler method for its discretization, i.e.,

$$\boldsymbol{E}\boldsymbol{x}_{k+1} = \boldsymbol{F}_k\boldsymbol{x}_k + \boldsymbol{B}\boldsymbol{u}_k + \boldsymbol{Q}\boldsymbol{w}_k \tag{9}$$

$$\boldsymbol{z}_k = \boldsymbol{H}\boldsymbol{x}_k + \boldsymbol{R}\boldsymbol{s}_k \tag{10}$$

where, for simplicity, $k := kT_s$ is the current discrete time in which T_s is the sampling time, $\boldsymbol{F}_k = \boldsymbol{E} + T_s\tilde{\boldsymbol{F}}_k$, $\tilde{\boldsymbol{F}}_k = \tilde{\boldsymbol{F}}(kT_s)$, $\boldsymbol{B} = T_s\tilde{\boldsymbol{B}}$, and $\boldsymbol{Q} = T_s\tilde{\boldsymbol{Q}}$.

The adopted state-space formulation of the LIM does not take into consideration the dynamic end effects and is therefore equivalent to the model of the RIM. The presence of the LIM dynamic end effects results in a variation of matrix $\boldsymbol{F}$: In particular, all of the electrical parameters vary with the machine speed; moreover, some additional terms are present with respect to the RIM equations (see [31] for the LIM modeling). In the proposed approach, the differences between the RIM model and the LIM model are in a way compensated by the KF.

The constants in these matrices have been selected on the basis of a trial-and-error method. To the best of the authors's capability, it has not been possible to find any studies in the scientific literature dealing with an analytical procedure for choosing a good set of numerical values. With regard to the numerical values of the $\boldsymbol{Q}$ matrix, the upper two values have been selected as ten times as big as the two lower ones. This is a crucial choice criterion for two reasons. First, the upper two diagonal terms of the $\boldsymbol{Q}$ matrix are related to the estimation of the inductor current components, which is the only portion of the state that is a measurable quantity; on the contrary, the lower two diagonal terms of the $\boldsymbol{Q}$ matrix are related to the induced part flux estimation, which is a nonmeasurable state variable. Since the error between the measured and estimated currents governs the closed-loop behavior of the KF, the components of the $\boldsymbol{Q}$ matrix related to the current must be as big as possible. On the contrary, since there is no feedback correction term on the induced part flux, the corresponding terms in the $\boldsymbol{Q}$ matrix should be lower. An overestimation of the noise effect on the estimation of the flux can lead to the instability of the observer. Second, this reason is related to the peculiar structure of the LIM with respect to the RIM. In the LIM case, the dynamics of the induced part flux is often faster than the one of the inductor currents (unlike the RIM case): This is caused by the presence of very high air-gap lengths and low values of thickness of the induced part track. This justifies the use of lower values for the two bottom values of $\boldsymbol{Q}$ to avoid unstable behaviors.

III. Formulation of the State Estimation Problem

In order to estimate the speed, two approaches can be employed.

The first approach considers the nonlinear model, which explicitly includes $v(t)$ as a state variable, and then uses an EKF [18] for estimating the state, with the use of the mechanical equation and under the assumption that load force t_l varies slowly. Thus, $\dot{t}_l = 0$ is added to the model of the motor, obtaining a sixth-order model. Another issue tied with the use of an EKF is that a linearized model is used instead of the real one. This approximation, sometimes, could lead to a failure for highly nonlinear systems, when the hypothesis of linearity in correspondence of the working condition is not valid.

The second approach, which is adopted in this paper, is based on the assumption that the speed is a parameter in (3) and (4) of the state model. This allows the states to be estimated by means of a recursive procedure in two steps. In the first step, for a given speed, state (flux and current), and input at the instant $k-1$, the induced part flux components at instant k are estimated using a linear fourth-order discrete-time KF, based on (9) and (10); in the second step, the speed is updated from the last two equations of (9), solving a TLS problem.

The block diagram of this described observer is shown in Fig. 1.

The advantage of the described procedure results in the reduction of the computational demand passing from a nonlinear sixth-order system to a linear fourth-order system by cascading a linear KF with an online speed estimator with increased computation efficiency. The sampling time that has been used is 10^{-4} s, by far lower than the mechanical time constant (about 5 s). This makes reasonable the assumption of smooth variation of the linear speed (assumed a parameter in (3) and (4) of the state model) between two time samples. In any case, this approach is supported by experimental results, where the system is able to work both at low and high speeds, as well as at zero speed (where EKF fails).

IV. Kalman Filtering for Flux and Current Estimation

If speed $\hat{v}_k$ is assumed known at instant k, the first step is the estimation of the state of the model (9) and (10) by means of a classical KF. It provides the optimal linear least mean squares estimate of the state variables given prior observations. (See the Appendix for a brief description of a linear KF.)

However, the classical algorithms(A1) and (A2) and (A7) and (A8) can be written in a different form by manipulating the equations and using the lemma of matrix inversion. This leads to the so-called descriptor-type KF [19], and the resulting recursive filtered estimate $\hat{\boldsymbol{x}}_{k|k}$ of the state $\boldsymbol{x}_k$ is given by

$$\hat{\boldsymbol{x}}_{k|k} = \boldsymbol{P}_{k|k}\Big[\boldsymbol{E}^T\left(\boldsymbol{Q}+\boldsymbol{F}_{k-1}\boldsymbol{P}_{k-1|k-1}\boldsymbol{F}_{k-1}^T\right)^{-1} \times\left(\boldsymbol{F}_{k-1}\hat{\boldsymbol{x}}_{k-1|k-1}+\boldsymbol{B}\boldsymbol{u}_{k-1}\right)+\boldsymbol{H}^T\boldsymbol{R}^{-1}\boldsymbol{z}_k\Big] \tag{11}$$

$$\boldsymbol{P}_{k|k} = \Big[\boldsymbol{E}^T\left(\boldsymbol{Q}+\boldsymbol{F}_{k-1}\boldsymbol{P}_{k-1|k-1}\boldsymbol{F}_{k-1}^T\right)^{-1}\boldsymbol{E} + \boldsymbol{H}^T\boldsymbol{R}^{-1}\boldsymbol{H}\Big]^{-1}. \tag{12}$$

At the instant $k=0$, the algorithm is initialized with (A10), where $\boldsymbol{z}_0=0$ and $\boldsymbol{P}_0=10\boldsymbol{I}_4$. With reference to the matrices $\boldsymbol{Q}$ and $\boldsymbol{R}$, the following choices have been made. Both $\boldsymbol{Q}$ and $\boldsymbol{R}$ have been chosen as constant diagonal matrices as follows:

$$\boldsymbol{Q}=\begin{bmatrix}0.02&0&0&0\\0&0.02&0&0\\0&0&0.002&0\\0&0&0&0.002\end{bmatrix},\quad \boldsymbol{R}=\begin{bmatrix}1&0\\0&1\end{bmatrix}.$$

The same matrices will be adopted in both simulation experimental tests.

The block diagram of the KF (11) and (12) is shown in Fig. 2.

Remark 5: Note that this algorithm requires the knowledge of $v(t)$ to build matrix $\boldsymbol{F}_k$.

Remark 6: The algorithm (11) and (12) is used in this paper according to the discrete mathematical model in a descriptor form (9) and (10) of the induction motor. It will be useful to build a robust version of this filter to take into account the parameter uncertainties, but as aforementioned, it will be considered in future work.

For other details about the theory and the implementation of this algorithm, the reader is addressed to [20].

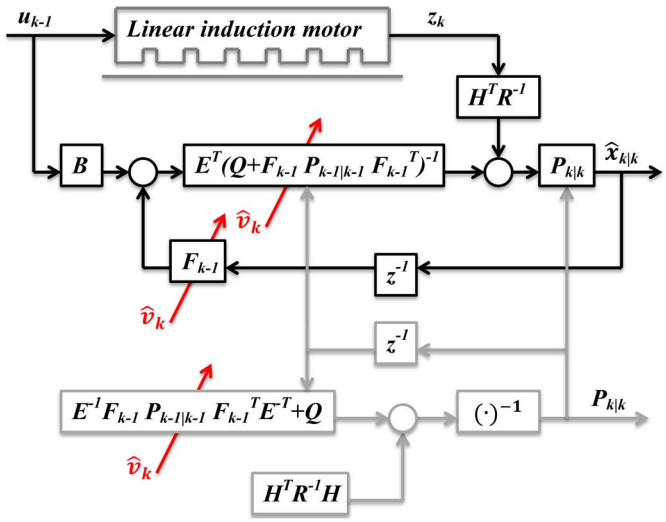

Fig. 2. Block diagram of the KF.

V. Speed Estimation

Using the Euler method for discretization, the last two equations of (9), expressing the dynamics of the induced part flux components, can be rewritten in the following matrix form:

$$\begin{bmatrix}-T_s\psi_{rq,k-1}\\T_s\psi_{rd,k-1}\end{bmatrix}p\frac{\pi}{\tau_p}v_{k-1}=\begin{bmatrix}\psi_{rd,k}-w_1\psi_{rd,k-1}-w_2 i_{sD,k-1}\\\psi_{rq,k}-w_1\psi_{rq,k-1}-w_2 i_{sQ,k-1}\end{bmatrix} \tag{13}$$

where $w_1=1-(1/T_r)T_s$ and $w_2=(L_m/T_r)T_s$, and the values of the induced part flux components are given from the solution of the first subproblem. From (13), the formulation of the second subproblem is as follows:

$$\min_{\hat{v}_k}\|\hat{\boldsymbol{\Phi}}_k\hat{v}_k-\hat{\boldsymbol{y}}_k\|^2 \text{ for } k\geq 0 \tag{14}$$

where

$$\hat{\boldsymbol{\Phi}}_k=p\frac{\pi}{\tau_p}\begin{bmatrix}-T_s\hat{\psi}_{rq,k-1}\\T_s\hat{\psi}_{rd,k-1}\end{bmatrix}$$

$$\hat{\boldsymbol{y}}_k=\begin{bmatrix}\hat{\psi}_{rd,k}-w_1\hat{\psi}_{rd,k-1}-w_2 i_{sD,k-1}\\\hat{\psi}_{rq,k}-w_1\hat{\psi}_{rq,k-1}-w_2 i_{sQ,k-1}\end{bmatrix}$$

are estimates of the flux components, and the measured currents are considered.

The problem (14) could be solved by means of ordinary least squares (OLS) method, but as is well known, the OLS method assumes that $\hat{\boldsymbol{\Phi}}_k$ is not affected by errors and all possible errors are confined to $\hat{\boldsymbol{y}}_k$. However, this hypothesis does not correspond to the real case because estimation and modeling errors lead up to errors also in $\hat{\boldsymbol{\Phi}}_k$. Thus, in this application, the adoption of TLS is better because it takes also into consideration the errors in the data matrix. As a consequence, instead of (14), a TLS problem should be solved, as shown in [9], by minimizing the following modified cost function:

$$\min_{\hat{v}_k}\frac{\|\hat{\boldsymbol{\Phi}}_k\hat{v}_k-\hat{\boldsymbol{y}}_k\|^2}{1+\hat{v}_k^2}. \tag{15}$$

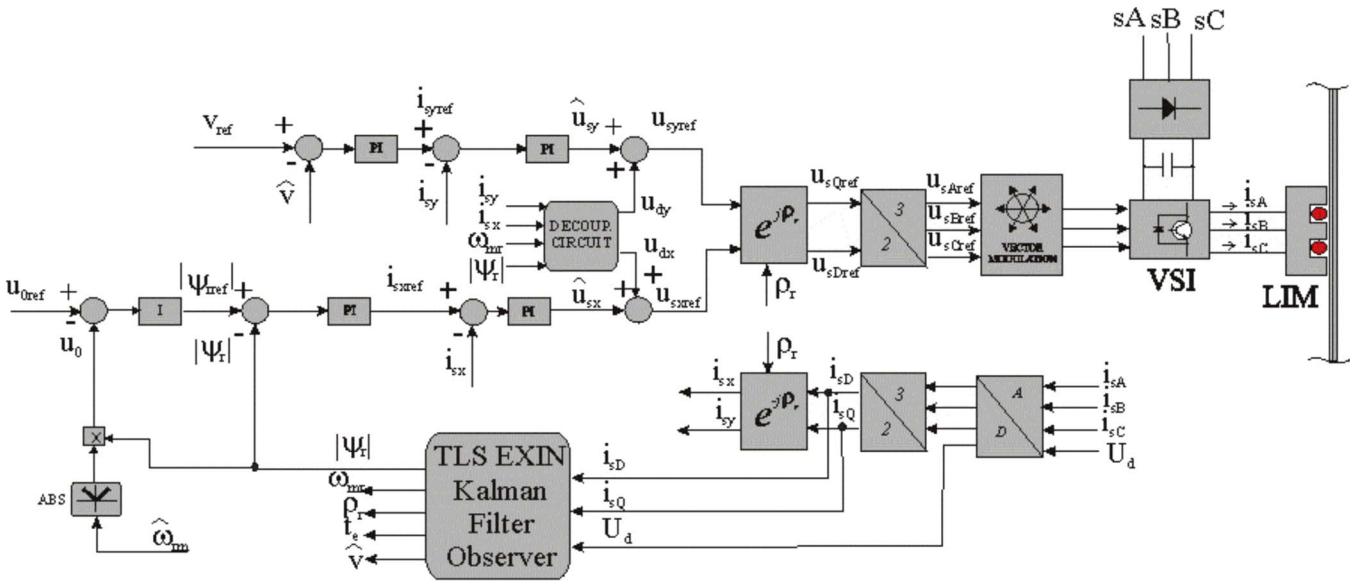

Fig. 3. Block diagram of the adopted control scheme.

The adaptation law that minimizes (15) is the TLS EXIN neuron shown as follows [10]:

$$\hat{v}_{k+1} = \hat{v}_k - \alpha_k \mathbf{\Gamma}_k^T \hat{\mathbf{\Phi}}_k + \alpha_k \hat{\mathbf{\Phi}}_k^T \hat{\mathbf{\Phi}}_k \hat{v}_k \tag{16}$$

where α_k is a positive constant, and $\mathbf{\Gamma}_k$ is given by

$$\mathbf{\Gamma}_k = \frac{\mathbf{\Delta}_k}{1+\hat{v}_k^2}, \quad \mathbf{\Delta}_k = \hat{\mathbf{\Phi}}_k \hat{v}_k - \hat{\boldsymbol{y}}_k.$$

In [10], it is proven that the origin $\hat{v} = 0$ always belongs to the convergence domain of TLS. Hence, the use of null initial conditions $\hat{v}_0 = 0$ is the best choice. With regard to the choice of the learning rate α in (16), the following criterion has been adopted. First, α is to be chosen so that the TLS neuron properly converges for each value of the LIM speed and for whatever speed transient of the drive while keeping the stability of the solution. This is usually guaranteed by choosing $\alpha < 1$. Another requirement for the proper choice of α is that the convergence speed (dynamics) of the TLS neuron must be as close as possible to the dynamics of the mechanical systems of the LIM. This means that the higher the mass of the inductor is, the lower the α that must be chosen. On this basis, trial-and-error procedures should be adopted to achieve the correct matching between the dynamics of the TLS and the mechanical system. In this application, a value of $\alpha = 0.1$ has been chosen.

VI. Description of the Sensorless Control System

The proposed control system is a direct induced-part-flux-oriented control of the LIM [21]–[24], [32]. The block diagram of the adopted control scheme is shown in Fig. 3, where current control is performed in the induced-part-flux-oriented reference frame (x, y). On the direct axis x, a flux control loop commands the direct current loop, and a voltage control loop commands the flux loop to permit the drive to work automatically in the field-weakening region. On the quadrature axis y, a speed loop controls the quadrature current loop. It should be noted that the angular position ρ_r, needed for the correct field orientation, is given by the TLS KF observer.

TABLE I
Parameters of the LIM

Rated power P_{rated} $[W]$	425
Rated voltage U_{rated} $[V]$	380
Rated frequency f_{rated} $[Hz]$	60
Pole-pairs	3
Inductor resistance R_s $[\Omega]$	11
Inductor inductance L_s $[mH]$	637,6
Induced part resistance R_r $[\Omega]$	32,57
Induced part inductance L_r $[mH]$	757,8
3-phase magnetizing inductance L_m $[mH]$	517,5
Rated thrust F_n $[N]$	62
Rated speed $[m/s]$	6,85
Mass $[kg]$	20

An asynchronous space-vector pulsewidth modulation (PWM) with $f_{\mathrm{PWM}} = 5$ kHz has been used to command the inverter. Finally, to cope with the inverter nonlinearity problem causing distortion and discontinuity of the inverter voltage vector with respect to the reference one, a methodology has been used that approximates every power device with a threshold voltage and a differential resistance [25], [26].

VII. Experimental Setup

A test setup has been suitably built to test the speed and flux observer described in Sections IV and V. The machine under test is a LIM model Baldor LMAC1607C23D99, whose rated data and electrical parameters are shown in Table I. The LIM has been equipped with a linear encoder Numerik Jena LIA series. The LIM presents an induced part track 1.6 m long. Fig. 4 shows a photograph of the test setup, which is made up of:

- a three-phase LIM with parameters shown in Table I;
- a frequency converter consists of a three-phase diode rectifier and a 7.5-kVA three-phase voltage source inverter;
- a dSPACE card (DS1103) with a PowerPC 604e at 400 MHz and a floating-point DSP TMS320F240.

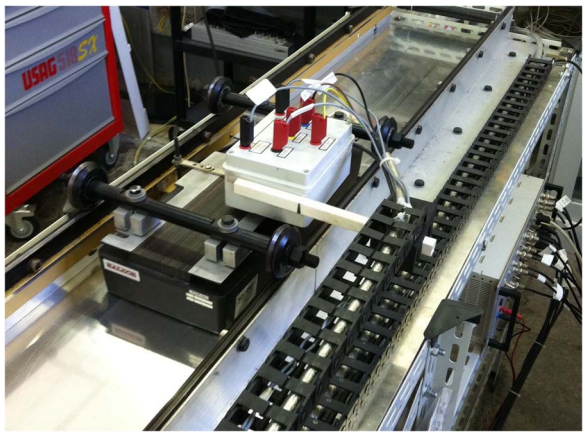

Fig. 4. Experimental rig.

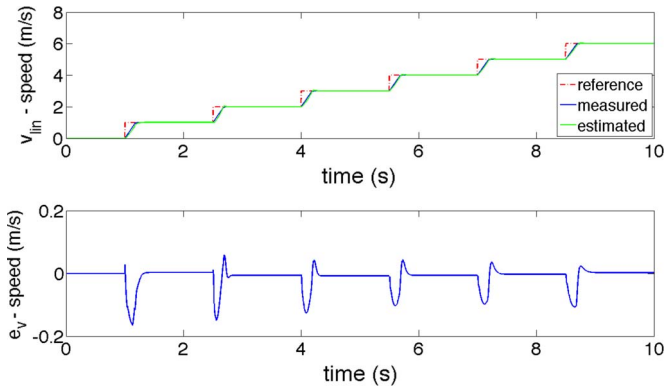

Fig. 5. TLS KF: Reference, estimated, and measured linear speeds during a variable speed test (simulation).

Both the estimator and the control are processed at 10 kHz. Finally, the data acquisition of the measurable variables and their visualization have been made using the DSpace software.

VIII. Simulation Results

The KF-TLS LIM sensorless drive has been tested in numerical simulation. It should be remarked that the simulation results are reliable even at high speed because the LIM model adopted as machine under test takes into consideration the LIM dynamic end effects [31].

In particular, some tests at working speed close to the rated one of the LIM can be made only on the numerical simulation because of the very short length of the track of the experimental setup (1.6 m). As a first step, a set of a speed step references from 0 to $1, 2, \ldots, 6$ m/s at no load has been given to the LIM drive. Fig. 5 shows the reference, estimated, and measured speeds and the speed estimation error (e_v as difference between the estimated and measured speeds). Fig. 6 shows the corresponding waveforms of the induced part flux amplitude and the electromagnetic force. These figures show that the speed estimation error is in average zero, even at rated speed, which is why a peak estimation error occurs at each speed step transient. The peak estimation error never exits 0.2 m/s. The thrust and flux waveforms exhibit a proper field orientation working conditions with flux corrected and controlled at a constant value and the thrust presenting step variations at each speed command.

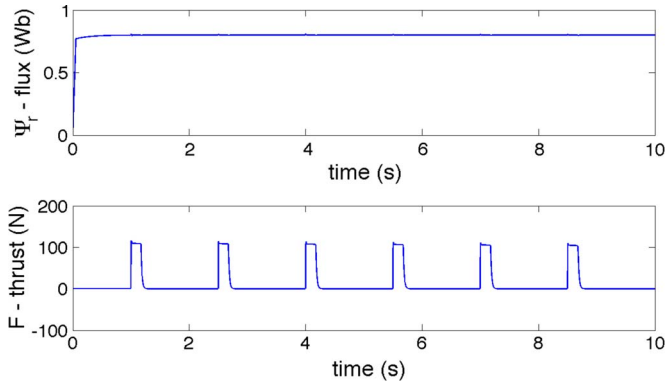

Fig. 6. TLS KF: Induced part flux amplitude and thrust during a variable speed test (simulation).

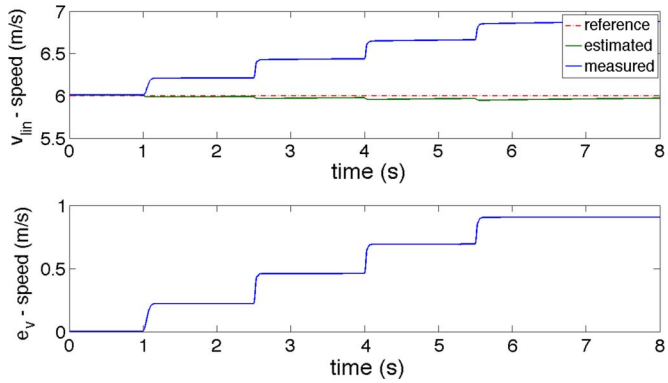

Fig. 7. TLS KF: Reference, estimated, and measured linear speeds during a load test (simulation).

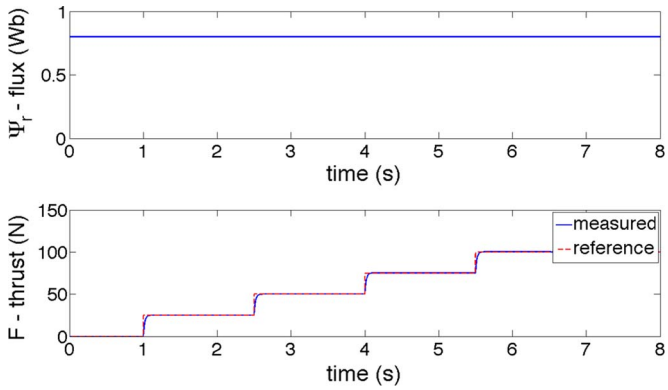

Fig. 8. TLS KF: Induced part flux amplitude and thrust during a load test (simulation).

As a second test, the drive has been given a constant speed reference of 6 m/s. At this speed, a set of subsequent step forces from 0 to 25, 50, 75, and 100 N has been given to the drive. Fig. 7 shows the set of speed waveforms, and Fig. 8 shows the corresponding waveforms of the induced part flux amplitude and the electromagnetic force. The speed waveforms show that the estimated speed is correctly controlled to the speed reference, whereas a bias in the speed estimation is present at load increasing with the force amplitude; this is the worst control condition since the machine works at a speed close to the rated one where the end effects are fully present whereas the observer model does not consider them. In this working condition, speed is less than 10%.

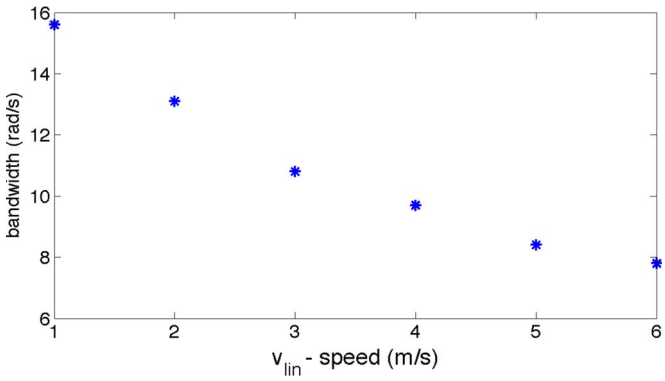

Fig. 9. Bandwidth versus the speed of the speed control loop.

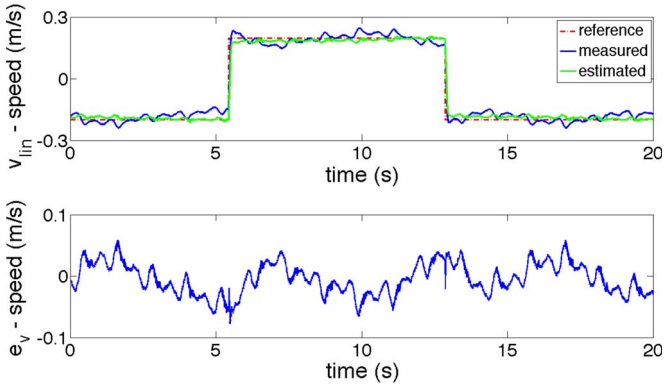

Fig. 10. TLS KF: Reference, estimated, and measured linear speeds during the $0.2 \rightarrow -0.2$ step (experiment).

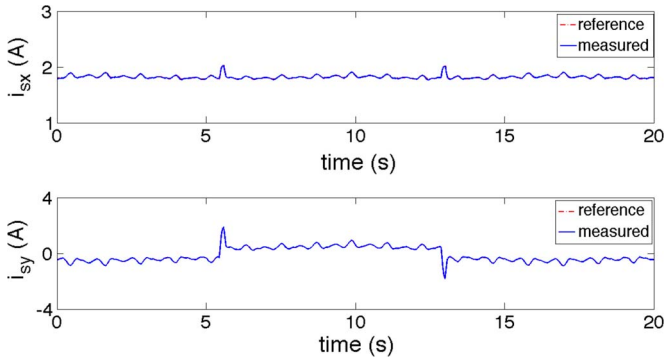

Fig. 11. TLS KF: i_{sx} and i_{sy} reference and measured current components during the $0.2 \rightarrow -0.2$ step (experiment).

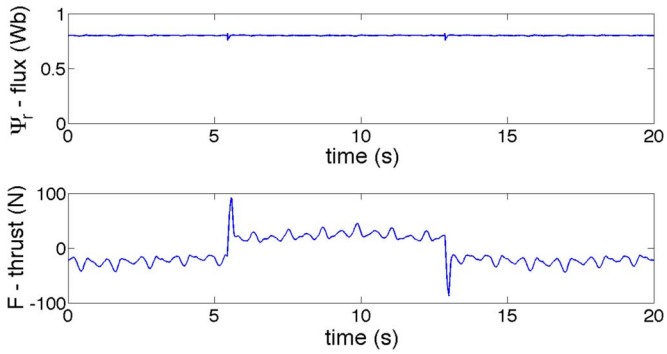

Fig. 12. TLS KF: Induced part flux amplitude and thrust during the $0.2 \rightarrow -0.2$ step (experiment).

With regard to the bandwidth of the speed control loop, it has been computed for several values of the working speed up to the rated speed. In this sense, the system has been assumed of the second order, and the corresponding formulas have been used to compute the bandwidth on the basis of the rise time and overshoot of the speed step. Fig. 9 reports this result. It confirms that the bandwidth of the speed loop reduces with increasing speed, which is to be expected since the rise time is higher at higher speed step.

IX. Experimental Results

The proposed TLS KF speed observer has been verified experimentally on the test setup described in Section VII. It has been verified in several challenging working conditions. In all the following tests, the estimated speed has been fed back to the speed control loop. The measured speed has been therefore used only for comparison reasons. The first test corresponds to a set of speed reversals at very low speed, from 0.2 to -0.2 m/s (rated linear speed of the LIM is 6.85 m/s), corresponding to almost 3% of the rated speed. The frequency of the square speed reference is implicitly determined by the length of the track: Whenever the inductor reaches the end of the track, the sign of the speed reference is changed.

Fig. 10 shows the reference, estimated, and measured speeds, as well as the speed estimation error (e_v as difference between the estimated and the measured speed) during the first test. The estimated speed properly tracks its reference, as expected. The measured speed correspondingly tracks the estimated one, even if with a transient estimation error (peak error almost equal to 0.05 m/s), depending on the inductor position on the track; it should be noted that, different from the RIM where the air gap can be considered almost uniform, in the LIM case, the air gap presents significant variations along its path. This last issue accounts for a different accuracy level of the speed estimation at steady state along the track obtained by several observers, as clearly shown in [8] and summarized in the following comparison section. Moreover, not only is the speed reference very low but also the LIM drive is actually loaded (almost 30% of the rated load) because of the friction force of the system due to the inductor rolling on the lateral tracks shown in Fig. 4. The reason why the experimental tests have been performed only with the friction load force is that, currently, the test setup is not equipped with any active load. To get around this problem, a corresponding numerical test has been performed (see Fig. 7). Fig. 11 shows the corresponding i_{sx} and i_{sy} current components, and Fig. 12 shows the induced part flux amplitude and the electromagnetic thrust. The inductor current curves highlight a proper field orientation, with i_{sx} correctly controlled to a constant value and i_{sy} suddenly varying at each speed reversal and controlled to a constant nonnull value at speed steady state (due to the load). Fig. 13 shows the i_{sD} and i_{sQ} current components in the inductor reference frame, respectively, estimated and measured, during the above test. An increase in the current component amplitudes can be noticed at the occurrence of each transient, as expected. The matching between the estimated and measured currents is good in both steady-state and transient conditions.

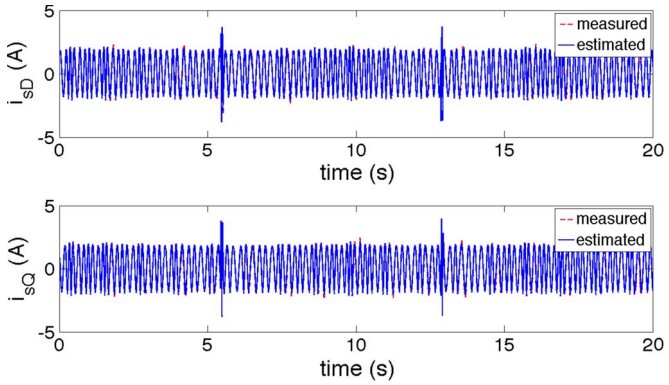

Fig. 13. TLS KF: Measured and estimated i_{sD} and i_{sQ} current components during the $0.2 \rightarrow -0.2$ step (experiment).

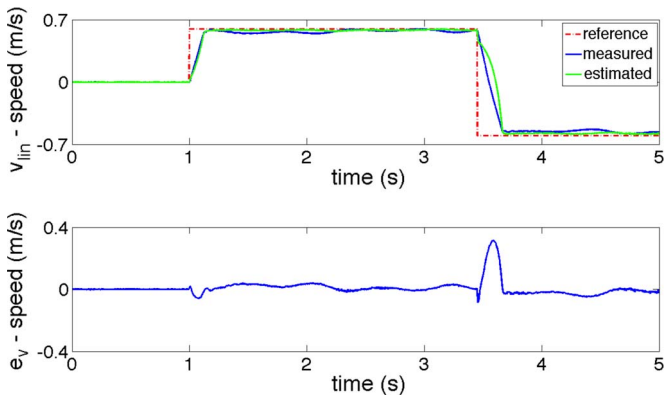

Fig. 14. TLS KF: Reference, estimated, and measured linear speeds during the startup test (experiment).

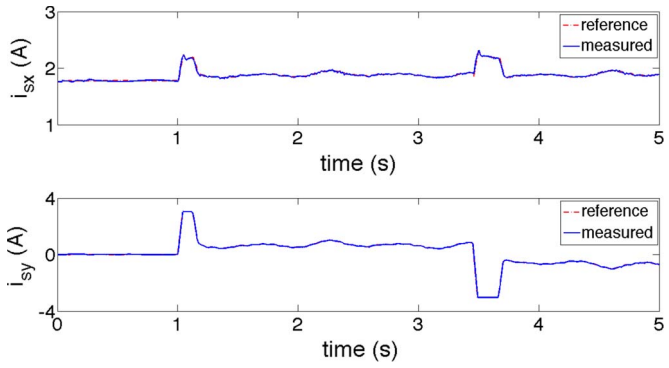

Fig. 15. TLS KF: $i_{sx}$and i_{sy} reference and measured current components during the startup test (experiment).

Afterward, two additional challenging tests have been made: 1) a startup plus speed reversal; and 2) a speed reversal plus braking. The startup test consists of the following speed step references $0 \rightarrow 0.6 \rightarrow -0.6$ m/s, whereas the braking one consists of the following speed step reference $0.6 \rightarrow 0$ m/s. These tests are particularly challenging since they imply a speed reversal at higher speed, a speed transient from/to zero speed, and a long period in which the drive is driven at zero speed with the LIM fully magnetized. Fig. 14 shows the reference, the estimated, and the measured speed as well as the speed estimation error during the startup test. Fig. 15 shows the corresponding waveforms of the reference and measured i_{sx} and i_{sy} current components. Fig. 16 shows the corresponding waveforms of

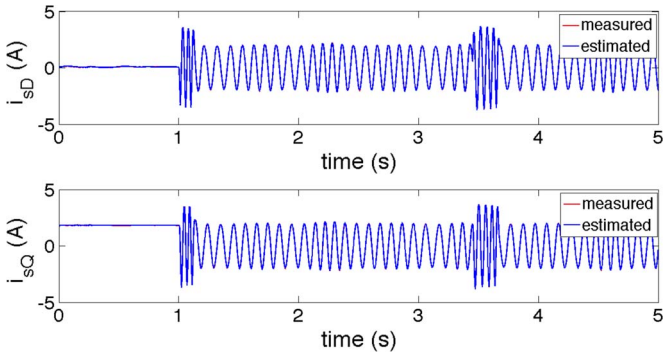

Fig. 16. TLS KF: Measured and estimated i_{sD} and i_{sQ} current components during the startup test (experiment).

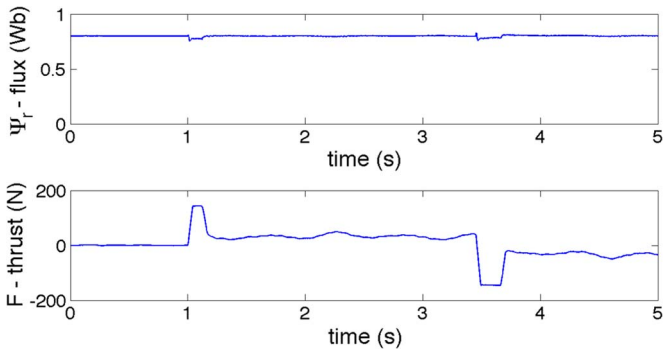

Fig. 17. TLS KF: Induced part flux amplitude and thrust during the startup test (experiment).

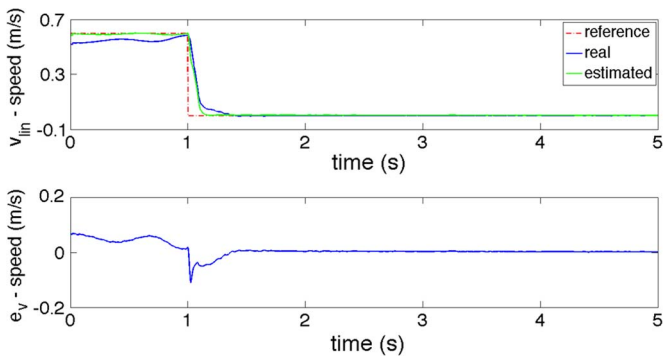

Fig. 18. TLS KF: Reference, estimated, and measured linear speeds during the braking test (experiment).

the measured and estimated $i_{sD}$and i_{sQ} current components. All the figures show the capability of the TLS KF observer to properly track these speed references with good accuracy even in transient while being able to work at zero speed with the machine fully magnetized. Moreover, the flux and thrust figures (see Fig. 17), as well as the corresponding current component ones, show very good dynamic performance as well as a proper field orientation (see Figs. 18–21 for the respective braking test counterparts of Figs. 14–17). Figs. 15 and 19 show that the estimated current components suitably track the measured ones, particularly in the phase of zero speed operation where the inductor current components become constant, and the machine model is theoretically unobservable.

However, it is well known that, in sensorless drives, the lower the working speed, the higher the presence of oscillation in

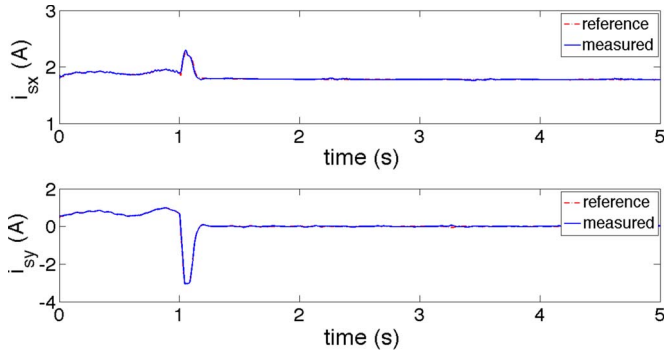

Fig. 19. TLS KF: $i_{sx}$and i_{sy} reference and measured current components during the braking test (experiment).

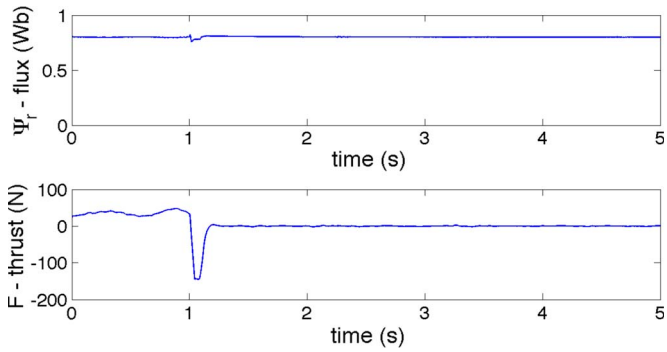

Fig. 20. TLS KF: Induced part flux amplitude and thrust during the braking test (experiment).

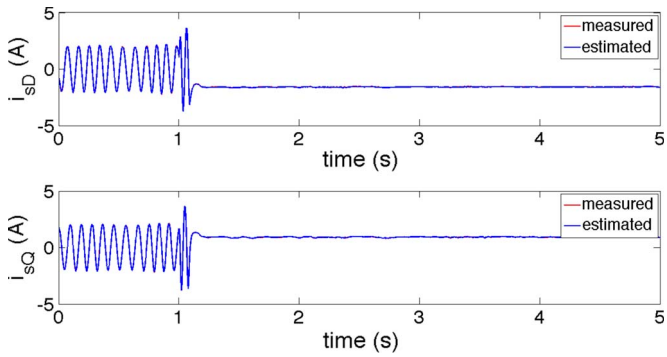

Fig. 21. TLS KF: Measured and estimated i_{sD} and i_{sQ} current components during the braking test (experiment).

electrical variables, because of the presence of nonlinear effects and machines parameter mismatch. This last effect explains the i_{sx} current component oscillating at low frequency, although the machine speed is constant; it is basically due to a nonperfect field orientation condition that is more visible close to zero speed.

Finally, it is useful to observe that there is a delay between the estimated and measured speed during the speed reversal from 0.6 and -0.6 m/s; this estimation error is typical of a sensorless drive, and it is particularly observable in LIM sensorless drives since the inversion of the motion is, in this case, even more critical than in the rotating counterpart (parameter variations with speed and friction load variation with speed). The higher the speed at which the reversal is made, the higher is the peak speed estimation error. This is the reason why the performance in Fig. 10 seems better. It should be in any case noticed that one of the advantages o the TLS EXIN speed is that it does not need any low-pass filter at the output. The TLS EXIN neuron behaves as a low-pass filter whose output can be directly fed to the speed control loop.

A. Comparison With the EKF

The proposed TLS KF has been experimentally compared with the classic EKF [27]. The EKF, as proposed in [27], different from the proposed TLS KF observer and the full-order Luenberger adaptive observer [28], assumes the speed as a state variable, whereas the full-order adaptive observer assumes it as a parameter. This means that the state matrix $\boldsymbol{F}$ is an augmented 6×6 matrix, with matrix $\boldsymbol{B}$ becoming a 6×2 matrix. In this way, the order of the state formulation increases from 4 to 6, with a consequent increase in the complexity and computation effort. The computational efficiency as a function of the dimensions of the state vector and of the measurement vector has been made by using the formulas shown in [20, Table 7.2]: The result is 984 operations for a fourth-order filter (TLS KF) and 1824 operations for a sixth-order filter (EKF). Thus, there is a meaningful increase in the computational efficiency just with the reduction of the order of the filter: The increase in computation from the TLS formula (16) does not affect this consideration since the TLS number of operations in this case is about 40. In other words, the number of operations is roughly decreased by 50%.

The main steps for the design of a speed sensorless induction-motor drive adopting an EKF are as follows [29]:

- selection of the time-domain induction machine model (in this case, the well-known space-vector model in state form of the RIM has been adopted);
- discretization of the induction machine model (details on the proper discretization methods are given in [29, p. 484];
- determination of the noise and state covariance matrices $\boldsymbol{Q}$ and $\boldsymbol{R}$ (in this case, these matrices are chosen equal to the KF adopted one);
- implementation of the discretized EKF and tuning.

The EKF has been implemented on the same test setup (see Section VII) where the TLS KF observer runs. In addition, in this case, the estimated speed has been fed back to the speed control loop; the measured speed has been therefore used only for comparison purposes. Also in this case, two tests have been made. The first is based on a square speed waveform with amplitude of 0.5 m/s. (For the same reason explained earlier, the frequency of the reference depends on the length of the track.) Fig. 22 shows the reference, measured, and estimated speeds, obtained with the EKF, under this test. It can be observed that the estimated speed properly tracks its reference with almost estimation error at steady state and limited peak error in transient state (almost 0.1 m/s). Even dynamic performance is satisfactory, showing a good field orientation condition, as visible from the i_{sx} and i_{sy} current waveforms (see Fig. 23) and in the same fashion from the induced part flux and thrust curves (see Fig. 24). Finally, Fig. 25 shows the measured and estimated i_{sD} and i_{sQ} current components. Moreover, in this case, there is a good matching between the estimated and the

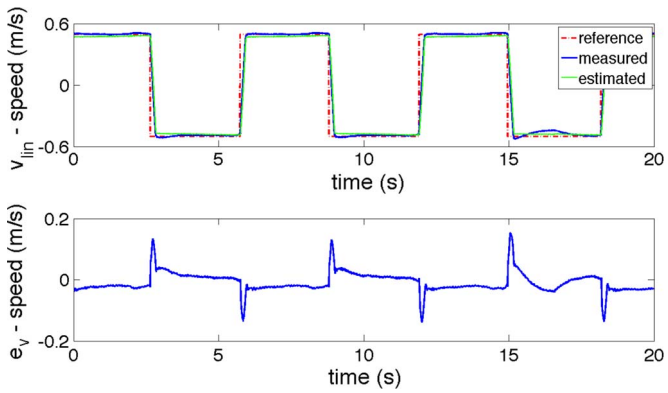

Fig. 22. EKF: Reference, estimated, and measured linear speeds during the $0.5 \rightarrow -0.5$ step (experiment).

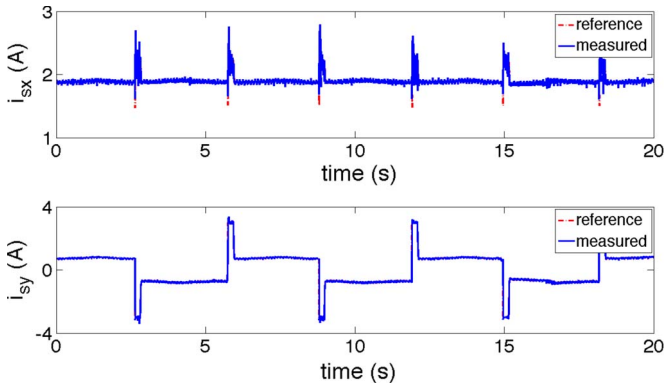

Fig. 23. EKF: i_{sx} and i_{sy} reference and measured current components during the $0.5 \rightarrow -0.5$ step (experiment).

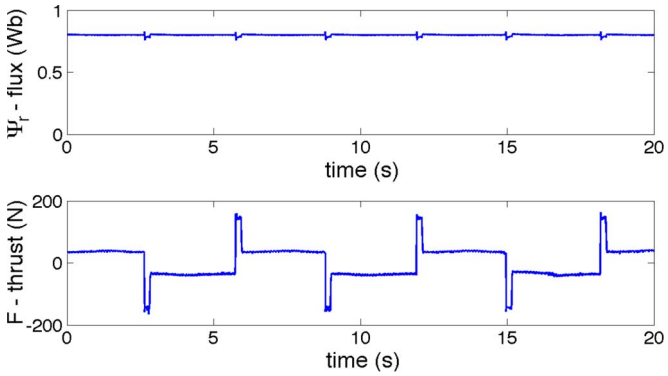

Fig. 24. EKF: Induced part flux amplitude and thrust during the $0.5 \rightarrow -0.5$ step (experiment).

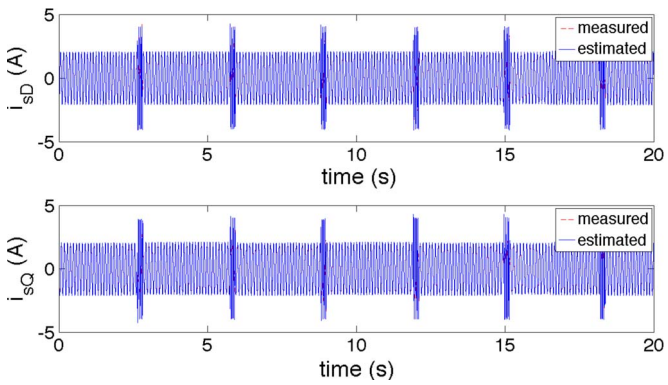

Fig. 25. EKF: Measured and estimated i_{sD} and i_{sQ} current components during the $0.5 \rightarrow -0.5$ step (experiment).

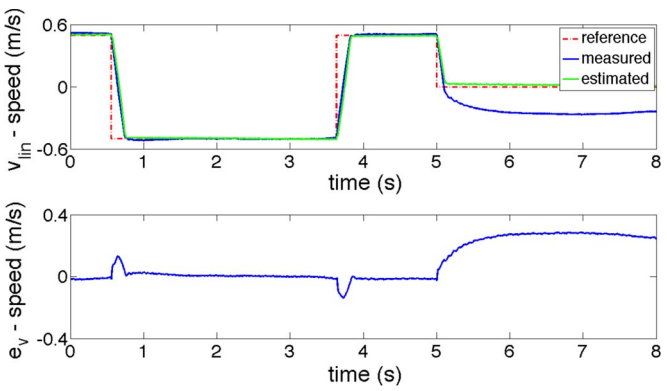

Fig. 26. EKF: Reference, estimated, and measured linear speeds during the braking test (experiment).

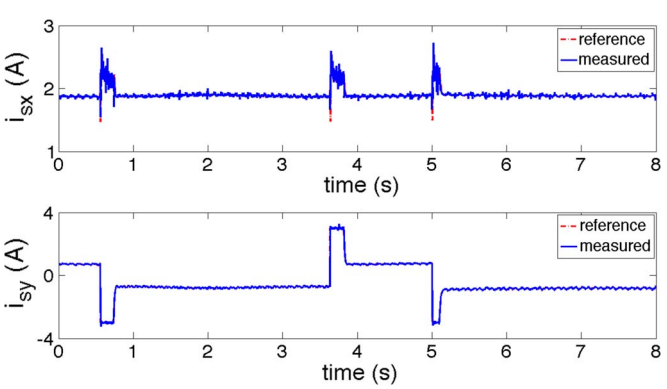

Fig. 27. EKF: i_{sx} and i_{sy} reference and measured current components during the braking test (experiment).

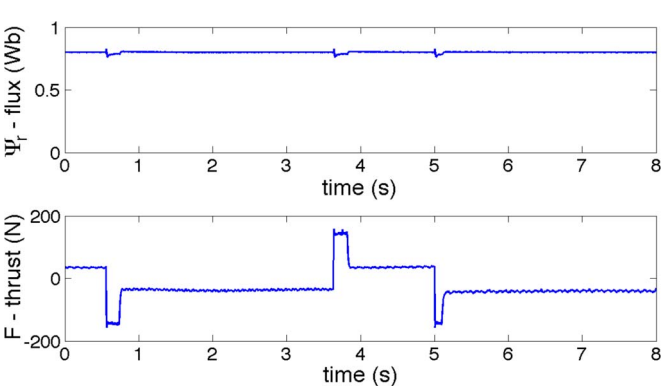

Fig. 28. EKF: Induced part flux amplitude and thrust during the braking test (experiment).

measured quantities, showing a proper working of the EKF. It should be noticed that 0.5 m/s is the minimum working speed of the EKF, in correspondence to which the behavior of the LIM drive is stable in sensorless operation. Below such a speed, the estimated speed still tracks its reference, whereas the measured speed becomes null. As a second test, the EKF LIM drive has been given a set of speed reversal from 0.5 to -0.5 m/s and vice versa, at the end of which a braking phase with a reference of zero speed is given. Figs. 26–29 show the same waveforms of the antecedent tests. It should be noted that the drive shows a proper behavior whenever the reference is nonnull. When the braking phase occurs and the reference speed becomes zero, the EKF LIM drive exhibits an unstable behavior.

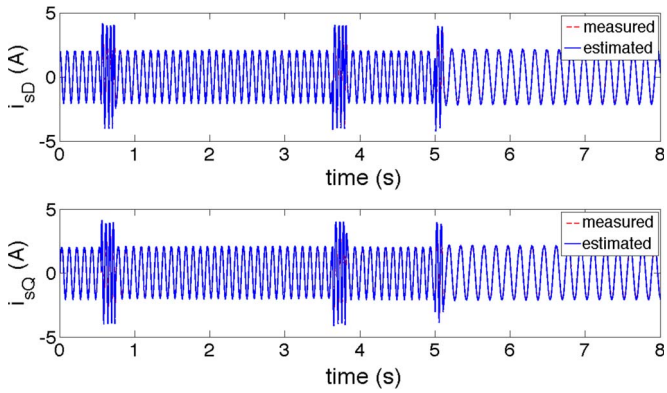

Fig. 29. EKF: Measured and estimated i_{sD} and i_{sQ} current components during the braking test (experiment).

TABLE II
COMPARISON BETWEEN TLS KF AND EKF

	TLS-KF	EKF
- minimum speed (% rated speed)	2.9%	7.4%
TEST AT 0.2m/s		
- speed mean error (%)	9%	NA
- speed peak error (%)	28%	NA
- speed standard deviation	$6.9 \cdot 10^{-3}$	NA
- speed relative deviation	$3.65 \cdot 10^{-2}$	NA
TEST AT 0.6m/s		
- speed mean error (%)	4%	5%
- speed peak error (%)	9%	8%
- speed standard deviation	$5.4 \cdot 10^{-3}$	$3.3 \cdot 10^{-3}$
- speed relative deviation	$9.2 \cdot 10^{-3}$	$-6.8 \cdot 10^{-3}$
- i_{sx} standard deviation	$4.7 \cdot 10^{-2}$	$2.2 \cdot 10^{-2}$
- i_{sy} standard deviation	$1.6 \cdot 10^{-1}$	$9.4 \cdot 10^{-2}$

Table II shows and compares the performance of the TLS KF and the EKF in terms of the minimum working speed (referred to the rated speed of the machine), the peak transient estimation error (referred to the reference speed), the steady-state percent average estimation error (referred to the reference speed), its corresponding standard deviation, and finally, the standard deviations of the direct and quadrature components of the inductor currents. These last two parameters take into consideration the oscillations typically occurring in the electrical variables in sensorless drives at low speed (with the estimated speed fed back to the control loop). As a final result, we have the following conclusions that can be carried out:

- Both the TLS KF and the EKF can work properly sensorless with the estimated speed fed back to the speed control loop. This is not the case for several speed observers (classic MRAS and SL-MRAS for example), as clearly shown in [8].
- The minimum working speed is obtained with the TLS KF: It corresponds to 2.9% of the rated speed, whereas the minimum working speed with EKF corresponds to 7.4% of the rated speed.
- At the minimum working speed, the average estimation error is 11% of the operation speed with the TLS KF and 6% of the operation speed with the EKF. The values of the average speed estimation errors are of the same order, slightly lower for the EKF, even if computed for each algorithm at its minimum working speed (2.9% of the rated speed for the TLS KF against 7.4% for the EKF).
- During the speed reversal at the minimum working speed, the lowest peak estimation error is 30% of the operation speed with the TLS KF and 27% of the operation speed with the EKF. Moreover, in this case, the peak estimation errors of the two algorithms are almost the same, even if computed at each corresponding minimum working speed.
- At the minimum working speed, the standard deviation obtainable of the i_{sx} (i_{sy}) current components is $4.7 \cdot 10^{-2}$ ($1.6 \cdot 10^{-1}$) with the TLS KF, and $2.2 \cdot 10^{-2}$ ($9.4 \cdot 10^{-2}$) with the EKF. Moreover, in this case, the current component standard deviations of the two algorithms are almost the same, even if computed at each corresponding minimum working speed.

X. CONCLUSION

This paper has proposed a state estimator for LIMs, which integrates a KF for the estimation of inductor currents and induced part flux linkage components, with a a speed estimator based on the TLS EXIN neuron. The TLS neuron, after receiving the state variables as inputs by the KF, provides as output the linear LIM speed that is fed back to the KF and the control system. The KF is based on the classic space-vector model of the RIM. The proposed TLS KF estimator has been tested experimentally on a suitably developed test setup, and it has been compared with the classic EKF. Results show that the TLS KF estimator permits the LIM drive to work down to 2.9% of the rated speed and even at zero speed, whereas the classic EKF works over 7.9% of the rated speed, and becomes unstable at zero speed.

Moreover, there is a meaningful increase in the computational efficiency just with the reduction of the order of the filter: It has been verified that the number of operations is roughly decreased by 50%.

APPENDIX A
LINEAR KF AND DESCRIPTOR-TYPE KF FUNDAMENTALS

The estimation of the state model uses a linear KF accomplished by a prediction phase, where the estimate of the state vector at instant k is made on the basis of the estimation of the previous instant $k-1$, and then by the innovation phase, where the kth prediction is updated and corrected on the basis of the kth measured value of the state vector. More precisely, these phases can be summarized as follows:

Prediction phase

$$\hat{\boldsymbol{x}}_{k|k-1} = \boldsymbol{E}^{-1}(\boldsymbol{F}_k \hat{\boldsymbol{x}}_{k-1|k-1} + \boldsymbol{B}\boldsymbol{u}_{k-1}) \tag{A1}$$

$$\boldsymbol{P}_{k|k-1} = \boldsymbol{E}^{-1}\boldsymbol{F}_k \boldsymbol{P}_{k-1|k-1}\boldsymbol{F}_k^T \boldsymbol{E}^{-1^T} + \boldsymbol{Q} \tag{A2}$$

where $\boldsymbol{P}_{k|k-1}$ is the *a priori* covariance matrix of the estimation error defined as

$$\boldsymbol{P}_{k|k-1} =: \mathbb{E}\left[(\boldsymbol{x}_k - \hat{\boldsymbol{x}}_{k|k-1})(\boldsymbol{x}_k - \hat{\boldsymbol{x}}_{k|k-1})^T\right] \tag{A3}$$

and $\boldsymbol{Q} = T_s\tilde{\boldsymbol{Q}}$ as defined in Section II. Note that, in this phase, only the *predicted values* of the state are used.

Innovation phase

In the innovation phase, the results obtained in the prediction phase are used. First, the e_k error between the measured currents $\boldsymbol{z}_k$ and the estimated currents $\boldsymbol{H}\hat{\boldsymbol{x}}_{k|k-1}$ is computed by using (A1)

$$\boldsymbol{e}_k = \boldsymbol{z}_k - \boldsymbol{H}\hat{\boldsymbol{x}}_{k|k-1}. \tag{A4}$$

Then, the innovation matrix $\boldsymbol{G}_k$ is computed by using (A2), i.e.,

$$\boldsymbol{G}_k = \boldsymbol{H}\boldsymbol{P}_{k|k-1}\boldsymbol{H}^T + \boldsymbol{R}. \tag{A5}$$

Matrix $\boldsymbol{G}_k$ is necessary to update the *optimal Kalman gain* $\boldsymbol{K}_k$ as follows:

$$\boldsymbol{K}_k = \boldsymbol{P}_{k|k-1}\boldsymbol{H}^T\boldsymbol{G}_k^{-1}. \tag{A6}$$

Once (A1), (A2), (A4), (A5), and (A6) are computed, the innovation phase can be accomplished with

$$\hat{\boldsymbol{x}}_{k|k} = \hat{\boldsymbol{x}}_{k|k-1} + \boldsymbol{K}_k\boldsymbol{e}_k \tag{A7}$$

$$\boldsymbol{P}_{k|k} = (\boldsymbol{I} - \boldsymbol{K}_k\boldsymbol{H})\boldsymbol{P}_{k|k-1} \tag{A8}$$

where $\boldsymbol{P}_{k|k}$ is defined as

$$\boldsymbol{P}_{k|k} =: \mathbb{E}\left[(\boldsymbol{x}_k - \hat{\boldsymbol{x}}_{k|k})(\boldsymbol{x}_k - \hat{\boldsymbol{x}}_{k|k})^T\right]. \tag{A9}$$

The algorithm is initialized with

$$\boldsymbol{P}_{0|0} = \left[\boldsymbol{P}_0^{-1} + \boldsymbol{H}^T\boldsymbol{R}^{-1}\boldsymbol{H}\right]^{-1} \quad \hat{\boldsymbol{x}}_{0|0} = \boldsymbol{P}_{0|0} + \boldsymbol{H}^T\boldsymbol{R}^{-1}\boldsymbol{z}_0 \tag{A10}$$

where $\boldsymbol{z}_0 = 0$, and $\boldsymbol{P}_0 = 10\boldsymbol{I}_4$.

In this paper, (11) and (12) are used, which represent the descriptor version of the classical KF derived in [19] by solving the following minimization problem:

$$\min_{\boldsymbol{x}_0}\left[\|\boldsymbol{x}_0\|^2_{\boldsymbol{P}_0^{-1}} + \|\boldsymbol{z}_0 - \boldsymbol{H}\boldsymbol{x}_0\|^2_{\boldsymbol{R}^{-1}}\right], \quad \text{for } k = 0 \tag{A11}$$

$$\min_{\boldsymbol{x}_k,\boldsymbol{x}_{k+1}}\left[\|\boldsymbol{x}_k - \hat{\boldsymbol{x}}_{k|k}\|^2_{\boldsymbol{P}_{k|k}^{-1}} + \|\boldsymbol{E}\boldsymbol{x}_{k+1} - (\boldsymbol{F}(\hat{v}_k)\boldsymbol{x}_k + \boldsymbol{B}\boldsymbol{u}_k)\|^2_{\boldsymbol{Q}^{-1}} + \|\boldsymbol{z}_{k+1} - \boldsymbol{H}\boldsymbol{x}_{k+1}\|^2_{\boldsymbol{R}^{-1}}\right], \quad \text{for } k > 0. \tag{A12}$$

The algorithm (11) and (12) can be considered the solution to a regularized least squares problem (see also [30, pp. 390–391,]) of the following form:

$$\min_{\boldsymbol{x}} = \left[\boldsymbol{x}^T\boldsymbol{U}\boldsymbol{x} + (\boldsymbol{A}\boldsymbol{x} - \boldsymbol{b})^T\boldsymbol{W}(\boldsymbol{A}\boldsymbol{x} - \boldsymbol{b})\right] \tag{A13}$$

where $\boldsymbol{x}^T\boldsymbol{U}\boldsymbol{x}$ is a regularization term, $\boldsymbol{U}$ is an orthogonal positive semi-definite weight matrix, and $\boldsymbol{W}$ is an orthogonal positive definite weight matrix, defined as

$$\boldsymbol{W} \leftarrow \begin{bmatrix} -\boldsymbol{Q}^{-1} & 0 \\ 0 & \boldsymbol{R}^{-1} \end{bmatrix}, \quad \boldsymbol{U} \leftarrow \begin{bmatrix} -\boldsymbol{P}_{k|k}^{-1} & 0 \\ 0 & 0 \end{bmatrix}. \tag{A14}$$

$\boldsymbol{x} \in \mathbb{R}^n$ is the unknown vector defined as

$$\boldsymbol{x} \leftarrow \begin{bmatrix} -\boldsymbol{x}_k - \hat{\boldsymbol{x}}_{k|k} \\ \boldsymbol{x}_{k+1} \end{bmatrix}. \tag{A15}$$

$\boldsymbol{A} \in \mathbb{R}^{N\times n}$ is the data matrix, and $\boldsymbol{b} \in \mathbb{R}^{N\times 1}$ is the observation vector, defined as

$$\boldsymbol{A} \leftarrow \begin{bmatrix} -\boldsymbol{F}_k & \boldsymbol{E} \\ 0 & \boldsymbol{H} \end{bmatrix}, \quad \boldsymbol{b} \leftarrow \begin{bmatrix} \boldsymbol{F}_k\hat{\boldsymbol{x}}_{k|k} + \boldsymbol{B}\boldsymbol{u}_k \\ \boldsymbol{z}_{k+1} \end{bmatrix}. \tag{A16}$$

Equation (A13) is equivalent to (A11) and (A12) by using (A14)–(A16). The solution of (A13) is

$$\hat{\boldsymbol{x}} = \left[\boldsymbol{U} + \boldsymbol{A}^T\boldsymbol{W}\boldsymbol{A}\right]^{-1}\boldsymbol{A}^T\boldsymbol{W}\boldsymbol{b}. \tag{A17}$$

Consequently, (A17) with the identifications, (A14)–(A16) lead to the time and measurement updates of the descriptor-type KF (11) and (12).

REFERENCES

[1] I. Boldea and S. Nasar, *Linear Electric Motors*, vol. 96. Englewood Cliffs, NJ, USA: Prentice-Hall, 1987, p. 97.

[2] I. Boldea and S. Nasar, *Linear Electric Actuators and Generators*. Cambridge, U.K.: Cambridge Univ. Press, 1987.

[3] K. Rajashekara, A. Kawamura, and K. Matsuse, *Sensorless Control of AC Motor Drives: Speed and Position Sensorless Operation*. New York, NY, USA: IEEE Press, 1996.

[4] J. Holtz, "Sensorless control of induction motor drives," *Proc. IEEE*, vol. 90, no. 8, pp. 1359–1394, Aug. 2002.

[5] C.-I. Huang, F. Li-Chen, W.-Y. Jywe, and J. C. Shen, "Speed motion-sensorless with adaptive control approach of linear induction motor unknown resistance and payload," in *Proc. IEEE PESC*, 2008, pp. 3887–3893.

[6] H.-M. Ryu, J.-I. Ha, and S.-K. Sul, "A new sensorless thrust control of linear induction motor," in *Conf. Rec. IEEE IAS Annu. Meeting*, 2000, vol. 3, pp. 1655–1661.

[7] M. Cirrincione, M. Pucci, A. Sferlazza, and G. Vitale, "Neural based mras sensorless techniques for high performance linear induction motor drives," in *Proc. 36th Annu. IEEE IECON*, 2010, pp. 918–926.

[8] A. Accetta, M. Cirrincione, M. Pucci, and G. Vitale, "Mras speed observer for high performance linear induction motor drives based on linear neural networks," *IEEE Trans. Power Electron.*, vol. 28, no. 1, pp. 123–134, Jan. 2013.

[9] G. Cirrincione and M. Cirrincione, *Neural-Based Orthogonal Data Fitting: The EXIN Neural Networks*, vol. 66. Hoboken, NJ, USA: Wiley, 2011.

[10] G. Cirrincione, M. Cirrincione, J. Herault, and S. Van Huffel, "The mca exin neuron for the minor component analysis," *IEEE Trans. Neural Netw.*, vol. 13, no. 1, pp. 160–187, Jan. 2002.

[11] M. Cirrincione, M. Pucci, G. Cirrincione, and G.-A. Capolino, "A new tls-based mras speed estimation with adaptive integration for high-performance induction machine drives," *IEEE Trans. Ind. Appl.*, vol. 40, no. 4, pp. 1116–1137, Jul./Aug. 2004.

[12] M. Cirrincione and M. Pucci, "An mras-based sensorless high-performance induction motor drive with a predictive adaptive model," *IEEE Trans. Ind. Electron.*, vol. 52, no. 2, pp. 532–551, Apr. 2005.

[13] M. Cirrincione, M. Pucci, G. Cirrincione, and G.-A. Capolino, "An adaptive speed observer based on a new total least-squares neuron for induction machine drives," *IEEE Trans. Ind. Appl.*, vol. 42, no. 1, pp. 89–104, Jan./Feb. 2006.

[14] M. Cirrincione, M. Pucci, G. Cirrincione, and G.-A. Capolino, "Sensorless control of induction machines by a new neural algorithm: The tls exin neuron," *IEEE Trans. Ind. Electron.*, vol. 54, no. 1, pp. 127–149, Feb. 2007.

[15] M. Cirrincione, M. Pucci, G. Cirrincione, and G.-A. Capolino, "Sensorless control of induction motors by reduced order observer with mca exin+ based adaptive speed estimation," *IEEE Trans. Ind. Electron.*, vol. 54, no. 1, pp. 150–166, Feb. 2007.

[16] F. Alonge, M. Cirrincione, F. D'Ippolito, M. Pucci, and A. Sferlazza, "Parameter identification of linear induction motor model in extended range of operation by means of input-output data," *IEEE Trans. Ind. Appl.*, vol. 50, no. 2, pp. 959–972, Mar./Apr. 2014.

[17] A. Accetta, M. Cirrincione, M. Pucci, and G. Vitale, "Neural sensorless control of linear induction motors by a full-order luenberger observer considering the end-effects," *IEEE Trans. Ind. Appl.*, vol. 50, no. 3, pp. 1891–1904, May/Jun. 2014.

[18] F. Alonge and F. D'Ippolito, "Extended kalman filter for sensorless control of induction motors," in *Proc. IEEE 1st Symp. SLED*, 2010, pp. 107–113.
[19] J. Y. Ishihara, M. H. Terra, and J. C. Campos, "Optimal recursive estimation for discrete-time descriptor systems," *Int. J. Syst. Sci.*, vol. 36, no. 10, pp. 605–615, 2005.
[20] M. S. Grewal and A. P. Andrews, *Kalman Filtering: Theory and Practice Using MATLAB*. Hoboken, NJ, USA: Wiley, 2001.
[21] J. Sung and K. Nam, "A new approach to vector control for a linear induction motor considering end effects," in *Conf. Rec. 34th IEEE IAS Annu. Meeting*, 1999, vol. 4, pp. 2284–2289.
[22] G. Kang and K. Nam, "Field-oriented control scheme for linear induction motor with the end effect," *IEE Proc. Elect. Power Appl.*, vol. 152, no. 6, pp. 1565–1572, 2005.
[23] V. Isastia *et al.*, "A voltage feeding algorithm for vectorial control of linear asynchronous machines taking into account end effect," in *Proc. Int. Conf. Power Electron. Drives Energy Sys. Ind. Growth*, 1998, vol. 2, pp. 729–734.
[24] I. Takahashi and Y. Ide, "Decoupling control of thrust and attractive force of a lim using a space vector control inverter," *IEEE Trans. Ind. Appl.*, vol. 29, no. 1, pp. 161–167, Jan./Feb. 1993.
[25] J. Holtz and J. Quan, "Sensorless vector control of induction motors at very low speed using a nonlinear inverter model and parameter identification," *IEEE Trans. Ind. Appl.*, vol. 38, no. 4, pp. 1087–1095, Jul./Aug. 2002.
[26] J. Holtz and J. Quan, "Drift-and parameter-compensated flux estimator for persistent zero-stator-frequency operation of sensorless-controlled induction motors," *IEEE Trans. Ind. Appl.*, vol. 39, no. 4, pp. 1052–1060, Jul./Aug. 2003.
[27] Y.-R. Kim, S.-K. Sul, and M.-H. Park, "Speed sensorless vector control of induction motor using extended kalman filter," *IEEE Trans. Ind. Appl.*, vol. 30, no. 5, pp. 1225–1233, Sep./Oct. 1994.
[28] H. Kubota, K. Matsuse, and T. Nakano, "Dsp-based speed adaptive flux observer of induction motor," *IEEE Trans. Ind. Appl.*, vol. 29, no. 2, pp. 344–348, Mar./Apr. 1993.
[29] P. Vas, *Sensorless Vector and Direct Torque Control*, vol. 729. Oxford, U.K.: Oxford Univ. Press, 1998.
[30] A. E. Bryson and Y. C. Ho, *Applied Optimal Control: Optimization, Estimation, and Control*. New York, NY, USA: Taylor & Francis, 1975.
[31] M. Pucci, "State space-vector model of linear induction motors," *IEEE Trans. Ind. Appl.*, vol. 50, no. 1, pp. 195–207, Jan./Feb. 2014.
[32] M. Pucci, "Direct field oriented control of linear induction motors," *Elect. Power Syst. Res.*, vol. 89, pp. 11–22, 2012

.

Francesco Alonge (M'02) was born in Agrigento, Italy, in 1946. He received the Laurea degree in electronic engineering from the University of Palermo, Palermo, Italy, in 1972.

Since then, he has been with the University of Palermo, where he is currently a Full Professor of automatic control with the Department of Electrical and Information Engineering and Mathematical Models. His research interests include electrical drive control (including also linear and nonlinear observers, stochastic observers, and parametric identification), robot control, parametric identification and control in power electronics, unmanned-aerial-vehicle motion control in aeronautics.

Maurizio Cirrincione (M'03–SM'10) received the Laurea degree in electrical engineering from the Polytechnic University of Turin, Turin, Italy, in 1991 and the Ph.D. degree in electrical engineering from the University of Palermo, Palermo, Italy, in 1996.

Since 1996, he has been a Researcher with the Institute of Intelligent Systems for Automation, Section of Palermo, National Research Council of Italy, Palermo. Since September 2005, he has been a Professor with the Université de Technologie de Belfort-Montbéliard, Belfort, France. His current research interests include neural networks for modeling and control, system identification, intelligent control, and electrical machines and drives.

Dr. Cirrincione received the E. R. Caianiello Prize for the best Italian Ph.D. thesis on neural networks.

Filippo D'Ippolito (M'00) was born in Palermo, Italy, in 1966. He received the Laurea degree in electronic engineering and the Research Doctorate degree in systems and control engineering from the University of Palermo, Palermo, in 1991 and 1996, respectively.

He is currently a Research Associate with the Department of Electrical and Information Engineering and Mathematical Models, University of Palermo. His research interests include control of electrical drives, adaptive and visual/force control of robot manipulators, and control of electrical power converters.

Dr. D'Ippolito received the 2000 Kelvin Premium from the Institution of Electrical Engineers, U.K., for the paper *Parameter Identification of Induction Motor Model Using Genetic Algorithms*.

Marcello Pucci (M'03–SM'11) received the Laurea and Ph.D. degrees in electrical engineering from the University of Palermo, Palermo, Italy, in 1997 and 2002, respectively.

In 2000, he was a Host Student with the Institute of Automatic Control, Technical University of Braunschweig, Braunschweig, Germany, working in the field of control of ac machines, with a grant from the German Academic Exchange Service. Since 2001, he has been with the Institute of Intelligent Systems for Automation, Section of Palermo, National Research Council of Italy, Palermo, where he is currently a Senior Researcher. His current research interests include electrical machines; control, diagnosis, and identification techniques of electrical drives; and intelligent control and power converters.

Dr. Pucci serves as an Associate Editor for the IEEE TRANSACTIONS ON INDUSTRIAL ELECTRONICS and IEEE TRANSACTIONS ON INDUSTRY APPLICATIONS. He is a member of the Editorial Board of the *Journal of Electrical Systems*.

Antonino Sferlazza (S'12) was born in Palermo, Italy, in 1987. He received the Master's degree in automation engineering from the University of Palermo, Palermo, Italy, in 2011. He is currently working toward the Ph.D. degree in system and control engineering in the Department of Electrical and Information Engineering and Mathematical Models, University of Palermo.

His research interests include the development of feedback control algorithms for nonlinear dynamical systems, optimization techniques and estimation of stochastic dynamical systems, and applications of control of electrical drives, power converters, and mechanical systems.

Gianpaolo Vitale (A'04–M'06–SM'12) received the Laurea degree in electronic engineering from the University of Palermo, Palermo, Italy, in 1988.

Since 1994, he has been with the Institute of Intelligent Systems for Automation, Section of Palermo, National Research Council of Italy, Palermo, where he has been a Senior Researcher since 2002. From 1999 to 2007, he was a Professor of power electronics and applied electronics with the Faculty of Engineering, University of Palermo. He was the Supervisor of a research project on electromagnetic compatibility of electric drives and of a research project on intelligent management of electric energy supplied by renewable sources. His current research interests include power electronics and related problems in electromagnetic compatibility.

Dr. Vitale is a member of the IEEE Vehicular Technology, IEEE Industrial Electronics, and IEEE Electromagnetic Compatibility Societies. He serves as a Reviewer for several journals and conferences.